THE JOURNAL OF PHYSICAL CHEMISTRY C

Article

pubs.acs.org/JPCC

Ultrafast Coherent Raman Scattering at Plasmonic Nanojunctions

Kevin T. Crampton,[†] Aram Zeytunyan,[†,∥] Alexander S. Fast,[†] Faezeh T. Ladani,[‡] Alba Alfonso-Garcia,[§] Mayukh Banik,[†] Steven Yampolsky,[†] Dmitry A. Fishman,[†] Eric O. Potma,*[,†] and V. Ara Apkarian*[,†]

[†]Department of Chemistry, [‡]Department of Electrical Engineering and Computer Science, and [§]Department of Biomedical Engineering, University of California, Irvine, California 92697, United States

ABSTRACT: Surface-enhanced coherent anti-Stokes Raman scattering (SECARS) measurements carried out on individual nanosphere dimer nantennas are presented. The ν-domain and t-domain CARS measurements in the few-molecule limit are contrasted as vibrational autocorrelation and cross-correlation, respectively. We show that in coherent Raman spectroscopies carried out with ultrashort pulses, the effect of surface enhancement is to saturate stimulated steps at very low incident intensities (100 fJ in 100 fs pulses), and the principal consideration in sensitivity is the effective quadratic enhancement of spontaneous emission cross sections, $\sigma^* = (E_L/E_o)^2\sigma$. Through multicolor femtosecond SECARS measurements we show that beside enhancement factors, an effective plasmon mode matching consideration controls the interplay between coherent electronic Raman scattering on the nantenna and vibrational Raman scattering on its molecular load. Through extensive measurements on individual nantennas, we establish the tolerable average and peak intensities that can be used in ultrafast measurements at nanojunctions, and we highlight a variety of plasmon-driven chemical and physical channels of signal and sample degradation.

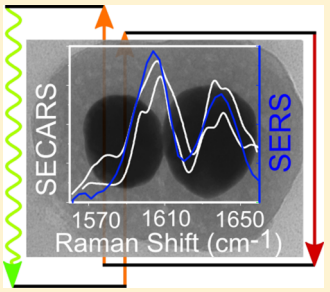

INTRODUCTION

Surface-enhanced Raman scattering (SERS), which takes advantage of plasmonic nanoantennas (nantennas) to enhance and confine fields, is an established method for performing vibrational spectroscopy in the single-molecule limit.[1−6] Conceptually, the technique is straightforward: properly designed nantennas allow convenient detection of the near-field molecular response with a far-field photodetector.[1,7] To clock vibrational motions of individual molecules in real time, it is necessary to rely on time-resolved (tr) nonlinear spectroscopy that uses at least two short laser pulses (pump and probe). The implementation requires the development of the surface-enhanced (SE) analog of ultrafast nonlinear spectroscopies. To this end, the response of plasmonic nantennas to ultrafast laser pulses and the coupling between the nantenna and its molecular load are critical considerations, which we address in the present work.

The SE effect, which is needed to raise radiative rates to detectable photon counts, can also be the demise of time-resolved measurements due to the very large local fields generated with short pulses. It was recently shown that under optimized conditions, molecular vibrational information is preserved when the conventional continuous wave (cw) illumination in SERS is replaced with short picosecond (ps) pulses.[8] In nonlinear coherent Raman, however, the combined molecule−nantenna system interacts with the multiple fields required to drive a given nonlinear process, and the resulting signal is often dominated by the nonlinear electronic response of the plasmonic nantenna itself. Although the electronic response of plasmonic nanostructures has been studied in the context of nonlinear optical interactions, including second harmonic generation (SHG),[9] sum-frequency generation (SFG), and four-wave mixing,[10−13] ultrafast studies that probe the molecular response mediated through the nantenna are few.[14]

The recent literature includes several accounts of surface-enhanced coherent anti-Stokes Raman scattering (SE-CARS)[2,15−21] and stimulated Raman scattering (SESRS)[7,22] experiments. In all of these cases, although short pulses are used, the measurements were carried out in the frequency domain. Frequency domain measurements contain information about the shortest time interactions that control ultrafast dynamics, and the existing examples suggest important differences between a given nonlinear scattering process and its SE analog. For example, the SESRS measurements on colloidal nanosphere dimers show dispersive vibrational lines.[22] In contrast, while heterogeneous ensemble SECARS studies report dispersive lineshapes,[23] SECARS on individual plasmonic nanostructures show nondispersive lines,[20] similar to those seen in cw-SERS. These observations contradict expectations based on standard implementations of SRS and CARS on ensembles. Because CARS is given as the square of the third-order polarization, it shows interference between the electronic continuum and discrete molecular transitions.[24] Along the same consideration, because SRS is proportional to the imaginary part of $P^{(3)}$, it does not heterodyne with the background. However, because the phase-shifted signal in SRS copropagates with the stimulating beam, interference is

Special Issue: Richard P. Van Duyne Festschrift

Received: March 16, 2016
Revised: April 22, 2016
Published: April 25, 2016

DOI: 10.1021/acs.jpcc.6b02760
J. Phys. Chem. C 2016, 120, 20943−20953

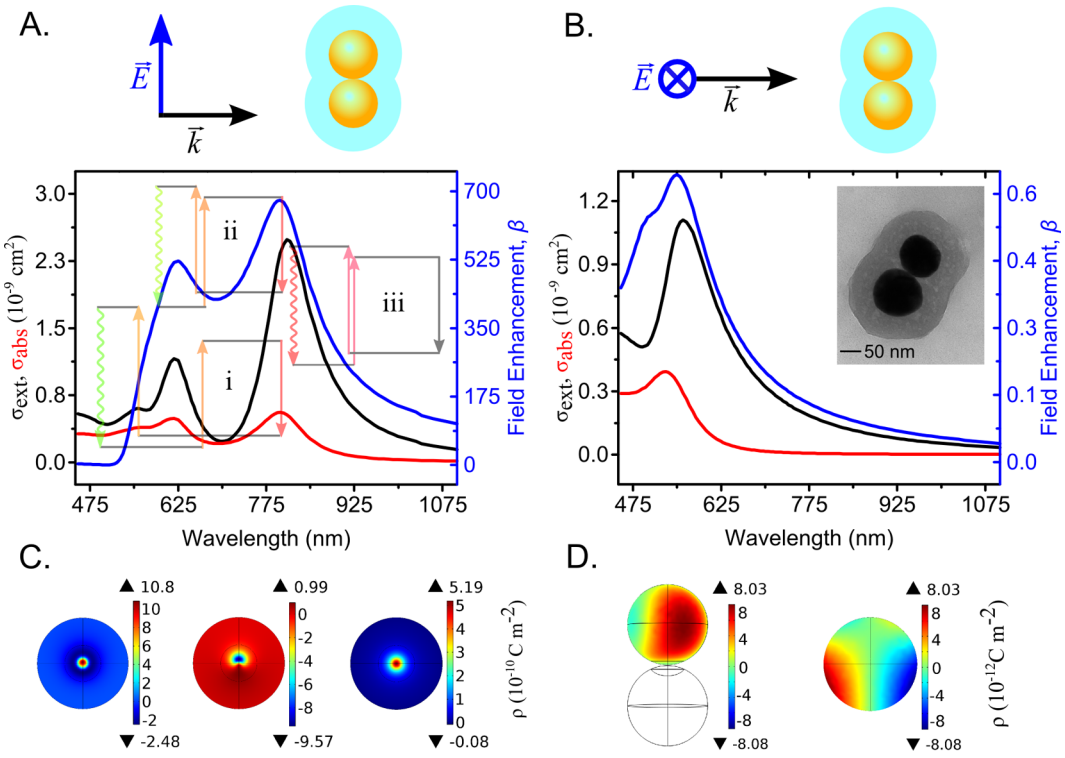

Figure 1. Linear spectral response of the nantenna for longitudinal (A) and transverse (B) excitation: extinction (black trace), absorption (red trace), and field enhancement factor (blue trace). Time circuit diagrams for the three SECARS measurements discussed are superposed over the spectra to highlight the resonances underlying the different excitations. They consist of (i) tr-SECARS executed with 100 fs pulses, using all three plasmon modes; (ii) previously reported[25] tr-SECARS utilizing the dipolar plasmon (pump and dump) and bonding quadrupolar resonances (probe and emission); and (iii) ν-domain SECARS using picosecond pulses, with all four waves coincident on the dipolar resonance. (C) Computed charge density distributions at the junction between the spheres for an applied field of 1 V/m at 555 nm (left), 618 nm (center), and 816 nm (right); (D) top and side views of the charge density for transverse excitation at 550 nm.

unavoidable. These considerations are less clear when the interaction with the molecular load is mediated via the nantenna, because now a new source of phase delay between molecule and plasmon is introduced. It is then valuable to compare SECARS versus SESRS carried out on the same plasmonic nanostructure and more generally to establish design considerations and fundamental limitations of time-resolved SE nonlinear optics (SE-NLO). As important is the distinction in information content of time domain versus frequency domain measurements using short pulses. These are the motivations behind the studies we report here.

We report on frequency domain SECARS measurements on the prototypical dumbbell nantenna consisting of a gold nanosphere dimer, the same system used in the reported SESRS measurements,[22] and on which we previously reported time-domain SECARS measurements using femtosecond (fs) pulses.[25] Be it in our prior t-domain measurements or the present ν-domain studies, the yield on single antennas is rather small. On the majority of interrogated dumbbells, the molecular signal fades before completion of the measurement. As we show, the dynamic range between detection and destruction of molecules via SE-NLO is rather narrow. The accumulated statistics of measurements carried out on several hundred individual dumbbells provides an exploration of the mechanisms of degradation, which can be distilled into fundamental limitations in SE-NLO measurements.

SYSTEM

A transmission electron micrograph of the typical dumbbell nantenna used in the present study is shown in the inset of Figure 1. It consists of two gold nanospheres, of ~95 nm diameter, separated by a junction gap of ~1 nm, and encapsulated in a silica shell of 40−70 nm thickness. The simulated linear spectral response of the idealized version of the same structure is presented in Figure 1 for two different incident $\vec{E}$ field polarizations. We present the extinction spectrum, the absorption spectrum, and the spectral dependence of the field enhancement in the middle of the intersphere junction, given by the ratio $\beta = E_L/E_0$ of local and applied field. Structural heterogeneity and variations in the gap length lead to large uncertainties in β which we address below through an exposition of the attainable count rates in cw and pulsed limits. Moreover, the gap dependence of these resonances has been recently reported.[26] The simulations are generally consistent with our measurements and will be used herein to quantify and rationalize observations. The nantenna sustains three major resonances that may be loosely assigned according to the commonly used hybridization model[27] to the bonding dipolar plasmon at 816 nm and the bonding and antibonding quadrupolar plasmons at 618 and 555 nm, respectively. Several observations are noteworthy at the outset. There is a dramatic difference in enhancement factors between longitudinal and transverse excitation. Only quadrupolar resonances are accessed in transverse excitation, in which case $\beta < 1$ at the intersphere junction, and surface charge density associated with the plasmon is broadly distributed on the dumbbell (Figure 1 D).

DOI: 10.1021/acs.jpcc.6b02760
J. Phys. Chem. C 2016, 120, 20943−20953

Also, scattering spectra are loosely correlated with the spectral dependence of β. This is clearest at 700 nm, which corresponds to the valley between scattering resonances (Figure 1 A), yet $\beta \sim 400$, not very different from the peak value $\beta \sim 700$ reached at 816 nm. Both values correspond to very large SERS enhancement factors of $\beta^4 \sim 10^{10}-10^{11}$. The apparent discrepancy is due to the fact that the extinction spectrum reflects the induced polarization integrated over the entire surface of the dumbbell, while the enhancement reflects the charge density concentrated at the junction (at the hot spot). The charge distributions promoted at the junction under the three longitudinal resonances are illustrated in Figure 1C. In contrast with the bonding dipolar plasmon, the charge density of the bonding quadrupolar plasmon is eccentric and π-phase shifted. These considerations become important in multicolor experiments that rely on multiple plasmon resonances. The finite element simulations we report in Figure 1 were carried out using the COMSOL multiphysics suite of programs, with the recently revised dielectric function of gold,[28] and the literature value of silica[29] as inputs.

Ideally, the nantenna serves as a silent mediator between the far-field and near-field radiation. However, in nonlinear optical measurements, electronic Raman scattering (ERS) of the metal and the coupled response of the molecule−metal system are integral parts of the observables. A synopsis of the information contained in cw-SERS spectra with regard to the interplay between molecular SERS and ERS of the nantenna is illustrated in Figure 2. The vibrational SERS of the reporter molecule, bipyridyl ethylene (BPE), can be seen to ride over a background continuum that can be rigorously assigned to ERS. The vibrational assignments have been reported previously,[30] and an analysis of the continuum was given recently.[31] Here, we note that the relative intensity of SERS and ERS depends on excitation wavelength and polarization angle. In longitudinal excitation, the ratio changes by a factor of ~20 between 532 and 633 nm, and the background becomes negligible at 785 nm (not shown). Transverse excitation at 532 nm shows ERS only, consistent with the fact that the accessed purely quadrupolar plasmon does not generate any significant fields at the intersphere junction (Figure 1B,D). This highlights that ERS arises from the net polarization induced on the nantenna, while SERS arises from the hot spot where the field is confined on a scale comparable to the molecular dimensions. In transverse excitation, the relative contributions of ERS and SERS scale by the spectral dependence of scattering and β, as discussed above. The clearest signature of ERS is the anti-Stokes branch of the continuum, which decays exponentially as a function of Raman shift.[31−33] It perfectly fits the Fermi−Dirac distribution of hole states, which serve as the thermally occupied terminal states in ERS (see Figure 2ii). The fit of the anti-Stokes ERS to the Fermi Dirac distribution yields the temperature of the nantenna, and its dependence on excitation intensity yields the heating rate, which limits the tolerable average irradiation intensity (see below). Remarkably, the vibrational anti-Stokes lines of the molecule, which can be seen at 633 nm, are completely absent when excited at 532 nm. This is ascribed to the competition between molecular SERS and molecule-to-metal scattering[31] with a real interfacial state resonance reached at 532 nm (Figure 2v). The continuum of final states in this scattering process explains the absence of sharp vibrational anti-Stokes lines.

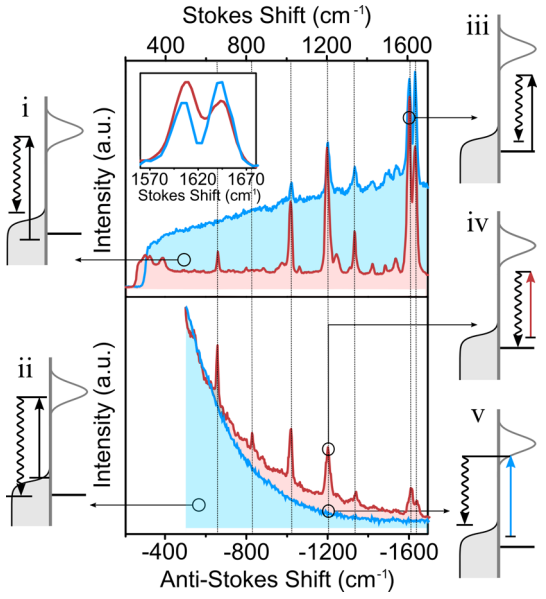

Figure 2. Stokes (top) and anti-Stokes (bottom) cw-SERS spectra recorded on a single nantenna at 532 nm (light blue trace) and 633 nm (red trace) excitation. Note the absence of vibrational lines in the anti-Stokes spectrum at 532 nm. Inset: Magnified C=C stretching modes at 1604 and 1640 cm^{-1} revealing Gaussian profiles of fwhm ~20 cm^{-1}. The various scattering contributions are indicated schematically: (i) Stokes of metal ERS; (ii) anti-Stokes ERS; (iii) Stokes of molecular SERS; (iv) anti-Stokes of molecular SERS, perfectly aligned with vibrational Stokes lines; and (v) absence of the molecular anti-Stokes lines at 532 nm, which is ascribed to the competition with molecule−metal scattering through the interfacial state resonance.

Although the location and number of molecules participating in scattering is not known, the absence of detectable SERS on single spheres establishes that the observed molecule(s) are near the hot spot of the junction in the dimer structures. Based on the known nonresonant Raman cross section of $\sigma_s = 5 \times 10^{-28}$ cm^2 for the strongest C=C stretching lines near 1600 cm^{-1} for BPE,[34] the observed count rates of 10^2-10^3 s^{-1} at an excitation intensity of 30 $\mu W/\mu m^2$ suggest an enhancement factor $\beta^4 = 10^8$ at 532 nm. Within the errors of this determination, the extracted local field enhancement of $\beta = 100$ agrees with the calculated value of 50 at 532 nm (Figure 1).

METHODS

ν-Domain SECARS. The system and methods employed in the ν-domain ps-SECARS studies that we report here are similar to those utilized in our prior t-domain measurements.[25] The main difference is the pulsewidth of the lasers. In the prior work, we used 100 fs pulses, with bandwidth sufficient to prepare the two bright C=C stretching modes at 1604 and 1640 cm^{-1} in superposition (Figure 2). We target the same vibrations in the present, now employing 7 ps pulses, with a bandwidth (6 cm^{-1}) much smaller than the ~35 cm^{-1} spacing between the lines. The measurements are carried out in imaging mode, using an optical microscope adapted to simultaneously measure cw-SERS and tr-SECARS (see Figure 3). The nantennas are dry-mounted on the SiN membrane (50 nm thick) of a transmission electron microscopy grid. They are first characterized and mapped-out via scanning electron microscopy then collocated on the optical microscope using backscattered light. A coincident pair of 76 MHz pulse trains is used for the ps-SECARS measurements: The 1064 nm output

DOI: 10.1021/acs.jpcc.6b02760
J. Phys. Chem. C 2016, 120, 20943−20953

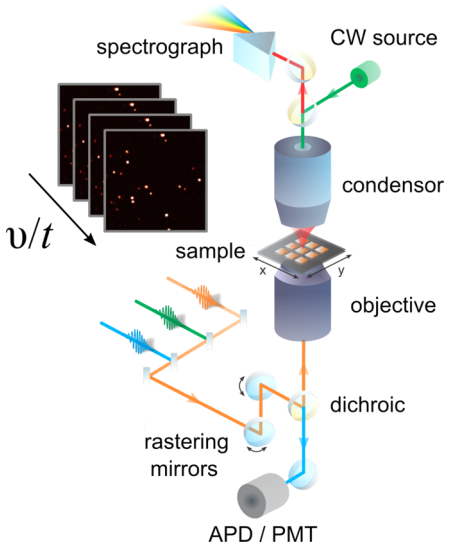

Figure 3. Schematic of the CARS microscope. Either galvo mirrors or a scanning stage are used to collect backscattered CARS images at each time delay, or at each frequency. The images are stacked to extract the photon count rate as a function of the dynamic variable (ν or t). The forward scatter channel is dedicated to cw-SERS, detected through a series of filters and a fiber-coupled spectrograph.

of a Nd:Vanadate laser (PicoTrain, High-Q) serves as the Stokes pulse, and a tunable optical parametric oscillator (Emerald OPO, A.P.E.), which is scanned from 905.0 to 913.5 nm with 0.5 nm steps, serves as pump and probe. The combination generates difference frequencies ranging from 1550 to 1660 cm^{-1}, which covers the spectrum of the bright C═C modes. The collinear beams are focused on the grid plane with a high NA objective (40× oil, 1.32 NA) in a laser-scanning inverted microscope (Fluoview 300, Olympus). At each frequency increment, a 92 × 92 μm^2 area of the grid is scanned with a dwell time of 10 μs/pixel (Figure 3). The approach allows the simultaneous interrogation of ∼50 dumbbells that fall within the scanned area. The anti-Stokes radiation is filtered (875 nm edge, 787 (22) bandpass; Semrock) and detected using a photomultiplier tube (R3896, Hamamatsu).

***t*-Domain SECARS.** We also carry out tr-SECARS measurements on individual nantennas using two different three-color, 100 fs sources, designed to carry out background-free measurements. The first consisted of two home-built noncollinear optical parametric amplifiers (NOPA), pumped with a 250 kHz regeneratively amplified Ti:sapphire laser (Mira Seed/REGA 9000, Coherent). The second consisted of an 79 MHz Ti:sapphire pumped photonic crystal fiber (PCF), tailor-made for SE-NLO.[35] As will be established below, the requirement for such measurements is an agile source of multicolor femtosecond pulses at high repetition rate and low intensity, with typical pulse energies of 100 fJ in 100 fs (100 μW at 100 MHz repetition rate). These specifications are based on fundamental limits in peak and average intensity that a nanojunction can tolerate, which we establish below. The limits are established by monitoring the molecular and nantenna response to ultrafast laser irradiation, through simultaneous measurements of the molecular SERS and the plasmon-enhanced electronic tr-CARS of the nantenna. Both sources were configured to prepare and probe the same vibrational superposition interrogated in the ps-SECARS experiments, following color scheme ii of Figure 1. An avalanche photodiode (SPCM-AQRH-25, Excelitas) or a photomultiplier tube (R6358, Hamamatsu) operating in photon counting mode is used for detection.

RESULTS AND DISCUSSION

ps-SECARS Spectra. ps-SECARS spectra recorded on six dumbbells are shown in Figure 4, along with the cw-SERS spectra recorded after the measurement on the same nantennas. Scanning electron micrographs recorded before and after the picosecond measurements did not show a noticeable change in the gross structure of these nanostructures. The recorded envelopes of the SECARS spectra can be seen to be in good agreement with those of the SERS, which exhibit Gaussian lineshapes of ∼20 cm^{-1} full width at half-maximum (fwhm). The noticeable difference is the jagged appearance of the SECARS spectra, due to under-sampling of the heterogeneous distribution betrayed by the Gaussian profiles. The cw-SERS spectra are recorded with 10 s exposure, during which the distribution is continuously sampled. The accumulated sampling time in the SECARS spectra is ∼1.5 ns per point (dwell time × rep rate × pulse width). Evidently, the sampling time in the ps-SECARS measurement is shorter than the time required to achieve ergodicity of the accessible phase space. Another important distinction is the contrast between the spectrum observed in the present ν-domain SECARS and the inferred spectrum from the prior t-domain measurement.[25] There, decoherence times as long as ∼10 ps were extracted for the two-state superposition, equivalent to a line width of ∼3 cm^{-1}. The discrepancy is understood by recognizing the unique difference in t- versus ν-domain measurements in the single-molecule limit. Recall that CARS measures the square of the third-order polarization:[36]

$$S(t) = |\int \mathrm{d}t\, \varepsilon(t) \sum_{\nu} a_{\nu} \exp(-\mathrm{i}(\omega_{\nu,0} + \Omega)t - \gamma_{\nu} t)|^2 \quad (1)$$

in which $\varepsilon(t)$ and Ω are the slow envelope and frequency of the probe pulse, and the summation is over the vibrational superposition prepared by the pump and Stokes pulses. With a pulse duration of 100 fs, much longer than vibrational periods $2\pi/\omega_{\nu,0}$ = 20 fs but shorter than the vibrational beat period $2\pi/(\omega_{\nu} - \omega_{\nu'})$ = 1 ps, the probe envelope acts as a time window that filters out only the difference terms $\omega_{\nu,\nu'} = |\omega_{\nu} - \omega_{\nu'}|$ in the product (eq 1).[37] This reduces the t-domain signal to the cross correlation between vibrations:

$$S(t) = \sum_{\nu,\nu'} a_{\nu} a_{\nu'} \exp(-\mathrm{i}(\omega_{\nu,\nu'})t - \gamma_{\nu,\nu'} t) \quad (2)$$

In contrast, line profiles in SERS, as in spontaneous Raman, reflect the autocorrelation of individual vibrations:

$$S(\omega) = |\int_0^{\infty} \mathrm{d}t\, \mathrm{e}^{-\mathrm{i}\omega t} \sum_{\nu} a_{\nu} \exp(-\mathrm{i}\omega_{\nu} t - \gamma_{\nu} t)| \quad (3)$$

The ν-domain SECARS spectrum recorded with a 7 ps probe pulse yields the Ω-shifted copy of the SERS spectrum, as seen in Figure 4 and predicted by eq 1. While not clear at the outset, we see that the ν-domain ps-SECARS recorded on a single nantenna does not contain information that is not already present in cw-SERS. In contrast with ensemble measurements, in the few-molecule limit, ν- and t-domain measurements are not simply Fourier related. In the present, the spectral covariance measured in t-domain is much smaller than the

DOI: 10.1021/acs.jpcc.6b02760
J. Phys. Chem. C 2016, 120, 20943−20953

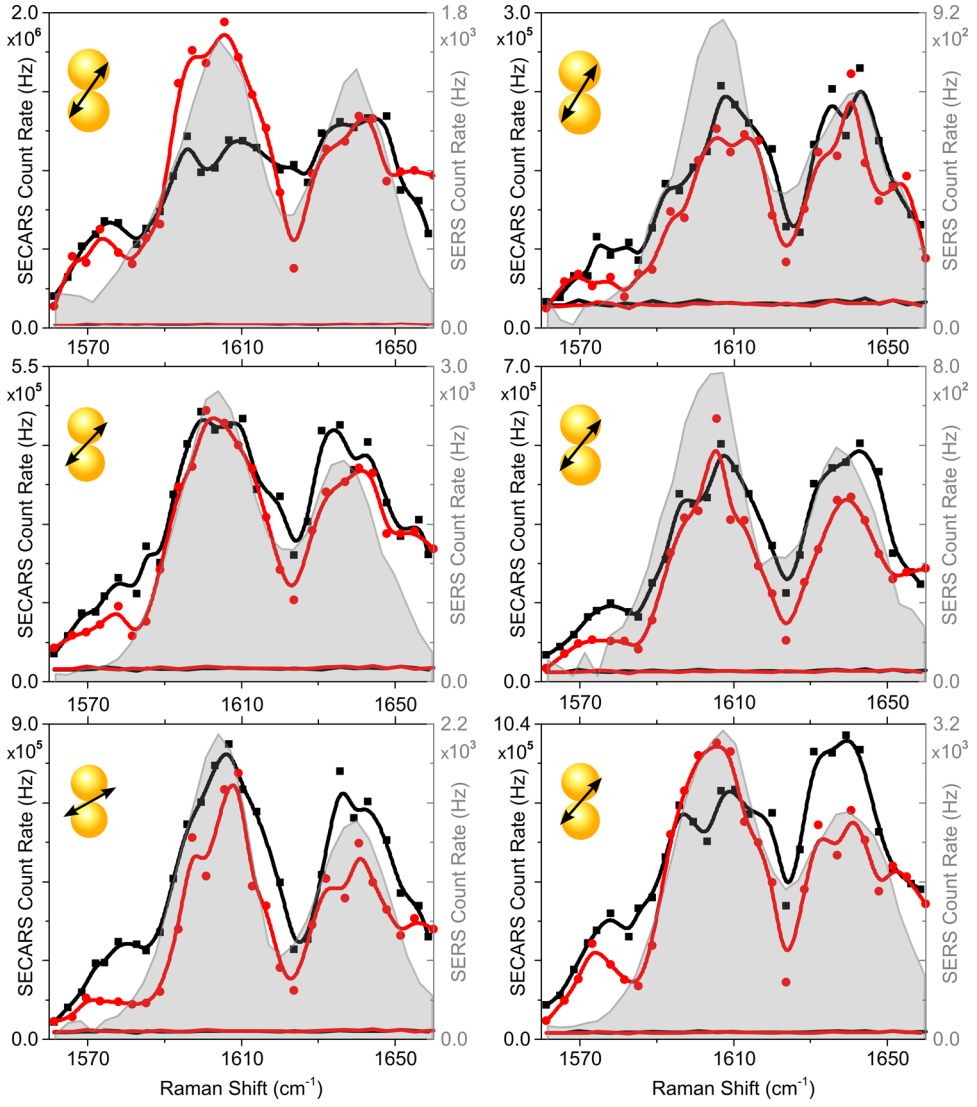

Figure 4. ps-SECARS spectra recorded on different dumbbells (red and black traces) and the cw-SERS spectra (gray, shaded) recorded on the same structures after the SECARS measurements. Consecutive SECARS measurements on each particle are reported: first acquisition in red and second acquisition in black. Also shown are the off-particle, background signals associated with each measurement. For the SECARS spectra, illumination conditions were as follows: $I_{Pu,i}$ = 525 μW/μm^2 and $I_{St,i}$ = 260 μW/μm^2 corresponding to peak incident intensities of 9 × 10^7 W/cm^2 and 5 × 10^7 W/cm^2, respectively. The relative orientation between laser polarization and nantenna is shown in the insets. The SERS spectra are recorded with a depolarized 633 nm cw laser (I_i = 10 μW/μm^2 = 1 × 10^3 W/cm^2).

variance observed in ν-domain spectral line widths. We may conclude that the two vibrations sample the broad inhomogeneous distribution in a highly correlated fashion, which implies that the two vibrations are driven by common environmental fluctuations. Moreover, the observation that ps-SECARS does not show any incremental broadening over SERS implies that the light-driven forces under the picosecond pulses are not perceivably different than in the case of cw illumination.

Measurement Yield. The data shown in Figure 4 are those of survivors, which represent ∼30% of the dumbbells imaged on the grid. The particles are randomly oriented on the grid, while the laser polarization is linear and fixed. Consistent with the strong dependence of enhancement factors on the polarization of the incident field (Figure 1), we find the modes of signal degradation on individual dumbbells to be correlated with their orientation on the grid. In Figure 5, we summarize measurements on 46 dumbbells by binning them into four categories: (i) The set of survivors, exemplified by the data in Figure 4, are dumbbells with long axis oriented at 45° ± 15° relative to the incident polarization. (ii) The set in which SECARS spectra decay during the course of measurement clump up near 30° ± 15°. The postmortem SERS spectra on these dumbbells are either very weak or strongly perturbed. In several cases, the BPE molecular lines are replaced by a new line at ∼2350 cm^{-1}, which we assign to CN and take as evidence for photodissociation of the pyridines. (iii) The set aligned near 17° shows strong electronic CARS void of any molecular signal. Their postmortem SERS is similar to the second category: we see either highly perturbed spectra or very weak BPE molecular features. (iv) Dumbbells that do not yield SECARS are either perfectly aligned with the *E*-field or perpendicular to it. The postmortem cw-SERS on the aligned nantennas is limited to ERS; the molecular SERS has entirely bleached. Nantennas that are perpendicular to the polarization retain an intact molecular SERS, reinforcing that the nanojunction is inaccessible in transverse pumping (see Figure 1).

DOI: 10.1021/acs.jpcc.6b02760
J. Phys. Chem. C 2016, 120, 20943−20953

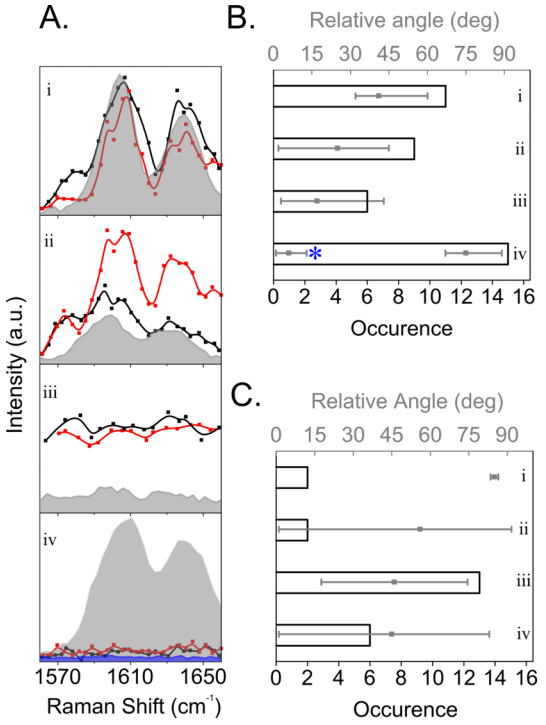

Figure 5. Statistics of survival organized in four categories, according to behavior illustrated in panel A by consecutively recorded ps-SECARS spectra (red and black traces for first and second acquistions) and subsequent cw-SERS (gray, shaded). The bar graphs show the correlation of the categories with orientation of the dumbbells relative to the polarization of incidence: (B) at peak pump and Stokes pulse intensities of 9×10^7 W/cm^2 and 5×10^7 W/cm^2; (C) the same correlation for a subsequent measurement when the intensities are increased to 5×10^8 W/cm^2 and 1×10^8 W/cm^2 for pump and Stokes, respectively.

Finally, the fraction of dumbbells that survive measurements is reduced from 30% to 8% upon doubling the intensity (see Figure 5 C). Because the enhanced local field changes dramatically with polarization angle of incidence, the observed orientation dependence confirms that rather than the incident field, it is the enhanced local field that induces degradation of the molecular SECARS signal. Yet, the local field, which plays the most critical factor in experimental considerations, is most difficult to quantify; hence, we rely on the computed values.

SERS versus tr-SERS Photon Yield. The limited dynamic range between damage threshold and detectability of the ultrafast measurements arises from the same enhancement factors that determine sensitivity. Recall that Raman is a feeble effect. The local field enhancement, $\beta = E_L/E_0$, provided by plasmonic nantennas is essential to boost its strength. The standard approximation of quartic field enhancement, the count rate, R, of spontaneously scattered photons in cw-SERS can be estimated as

$$R_{\text{cw-SERS}} = \frac{\eta}{\hbar\omega_i}(\beta_i^2 I_i)(\beta_s^2 \sigma_s) = \frac{\eta}{\hbar\omega_i} I_L \sigma_s^* \tag{4}$$

in which η is the collection efficiency (~0.1 under optimized geometries); I_i (W/cm^2) is the incident field intensity; σ_s(cm^2) is the spontaneous scattering cross section; and the subscript on β indicates its wavelength dependence. We have grouped the enhancement factors to recognize that the effect in $I_L = \beta_i^2 I_i$ is to reduce the demand on incident intensity. Because there usually is a reserve of incident laser intensity in typical pulsed setups, the fundamental advantage in tr-SERS reduces to the quadratic enhancement of the cross section $\sigma_s^* = \beta_s^2 \sigma_s$.

For tr-SERS, the count rate is determined by the peak intensity I_L^{peak} and fill factor ff = $f\delta t$, given by the product of laser repetition frequency, f, and pulse width, δt:

$$R_{\text{tr-SERS}} = \frac{\eta}{\hbar\omega} I_L^{\text{peak}} \sigma_s^* \text{ff} \tag{5}$$

At a repetition rate of 76 MHz and pulse width of 7 ps, ff = 5×10^{-4}. To compensate for the fill factor, the peak intensity in the pulsed measurements must be increased by 4 orders of magnitude. Given typical intensities used in cw-SERS of 10^4 W/cm^2 (at 532 nm), the required incident peak intensity is $I_L^{\text{peak}} \sim 10^8$ W/cm^2. This is the intensity used in the above-reported ps-SECARS measurements, where we have seen that we are within a very narrow window of the damage threshold. Using the computed value of $\beta_i \sim 3 \times 10^2$ at 900 nm, we deduce the tolerable local field intensity to be $I_{L,\text{max}}^{\text{peak}} < 10^{13}$ W/cm^2.

Saturation of Stimulated Steps in tr-SECARS. The tr-SERS signal considered in eq 5 is for spontaneous Raman (SR), a two-photon process in which a pump photon is absorbed and a Stokes photon is emitted. CARS is a four-photon process, which can be decomposed into stimulated Raman scattering (SRS) followed by SR. The expected SECARS count rate may be expected to scale as

$$R_{\text{SE-CARS}} \propto (\beta_{\text{Pu}}^2 I_{\text{Pu}})(\beta_{\text{St}}^2 I_{\text{St}})(\beta_{\text{Pr}}^2 I_{\text{Pr}})(\beta_{\text{As}}^2 \sigma_{\text{As}}) \tag{6}$$

The first two terms on the right-hand side in 6 correspond to SRS, whereas the last two terms represent spontaneous anti-Stokes Raman. Coherence among scatterers that distinguishes CARS in ensembles is irrelevant in measurements on single scattering centers. As such, the second step in CARS scales with the rate of SR, but now acting on the vibrationally excited molecule(s) prepared through SRS. Therefore, the photon yield in tr-SECARS must be reduced relative to tr-SERS by the efficiency of the initial SRS process. Yet, the photon count rates of 10^5–10^6 Hz seen in the ps-SECARS in Figure 4 are 2–3 orders of magnitude larger than the cw-SERS count rates. Even after making due allowance for differences in β-values and ff, the ps-SECARS counts remain 1–2 orders of magnitude larger. This necessarily implies that the stimulated steps in SECARS are near saturation. The same conclusion can be reached by noting that the rate of stimulated versus spontaneous radiation scales by the occupation number of photons, n, in the stimulating mode:[38]

$$\frac{R_{\text{SRS}}}{R_{\text{RS}}} = \frac{(n+1)}{1} = n \tag{7}$$

Even if we ignore mode confinement by the nantenna, the typical number of incident photons per pulse of $n = 10^7$ can be expected to amplify the observed SERS count rate $R_{\text{RS}} \sim 10^3$ s^{-1} to an SRS rate of $R_{\text{SRS}} = 10^{10}$ s^{-1}. This is 2 orders of magnitude larger than the repetition rate of the laser. As such, we may safely assume that the interrogated vibrational coherence is prepared with every pulse, i.e., the SRS step is saturated. Recent reports, which demonstrate SRS saturation of electronically nonresonant molecules at peak intensities of ~10^{11} W/cm^2, echo this conclusion.[39] The applicability of eq 5 to tr-SECARS is contingent on saturation of the stimulated steps, which is verified by the count rates seen in SERS and SECARS as a function of ff.

DOI: 10.1021/acs.jpcc.6b02760
J. Phys. Chem. C 2016, 120, 20943–20953

Plasmon Mode Matching. In two-color tr-CARS measurements, where the pump and probe pulses are derived from the same laser, there is an unavoidable background that arises from the coincidence of all three pulses at $t = 0$. This can be overcome in 3-color measurements, with distinct Pu, St, and Pr colors, hence a unique (background-free) 4-wave mixing that generates the targeted AS signal. This was accomplished by two different 3-color, 100 fs laser systems, operating at 79 MHz and 250 kHz, respectively. In the case of the 250 kHz system, the dramatic reduction in fill factor ff = 2.5×10^{-8} makes tr-SECARS measurements on single scattering centers rather challenging. Nevertheless, because of the reduction in background, tr-SECARS measurements could be done with results identical to those observed at 79 MHz. The observed tr-SECARS signal is shown in Figure 6. It consists strictly of the instantaneous response of the anti-Stokes ERS of the nantenna, with no trace of the time-delayed molecular signal. This is in stark contrast with the ps-SECARS data in Figure 4, where the molecular signal appears with negligible ERS background. The colors used in these measurements are contrasted with those of the ps-SECARS measurements against the backdrop of the nantenna resonances in Figure 2.

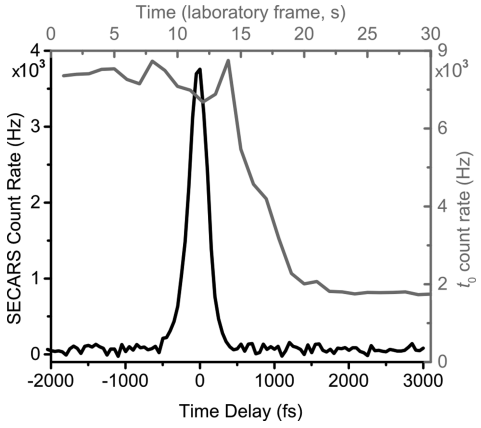

Figure 6. Time-resolved signal (black trace) from a dumbbell obtained through 3-pulse, 3-color CARS (scheme i in Figure 1), illustrating the metal response at $t = 0$ and the absence of a molecular signal at positive time. Gray curve: The time course of the $t = 0$ response of a dumbbell decays after an induction period of ~15 s, suggesting collapse of the nanojunction.

Consistent with all stimulated steps being saturated, the observed count rate in the fs-tr-SECARS signal (Figure 6) can be directly related to the ps-SECARS count rates (Figure 4) through eq 5. Using the computed enhancement factors, the relative ratio of spontaneous scattering rates alone, $(\beta_{AS}{}^2\text{ff}/\beta_{AS'}{}^2\text{ff}') \sim 2 \times 10^3$, rationalizes the observed ratio of count rates between the picosecond and femtosecond measurements. The contrast of seeing strictly molecular response in the 2-color experiment and strictly ERS of the nantenna in the 3-color experiment underscores that enhancement factors alone do not determine the signal in CRS mediated via the nantenna. Plasmon mode matching is an important consideration. As in the prior femtosecond tr-SECARS measurements, the present ps-SECARS data were obtained with all four waves coupled through the bonding dipolar plasmon. The three-color femtosecond SECARS relies on the bonding dipolar plasmon to prepare the coherence, the bonding quadrupolar plasmon to probe, and the antibonding quadrupolar plasmon to enhance the anti-Stokes signal (see Figure 2). As in the cw-SERS spectrum of Figure 2, where the molecular anti-Stokes scattering is completely absent at 532 nm, here too we see only the ERS of the metal. The opening of the molecule-to-metal scattering channel, which shows strong nonlinearity,[31] is operative in the 3-color experiment. This dramatic difference in observables can be generally ascribed to the requirements of plasmon mode matching in nantenna-mediated preparation and interrogation of molecular coherences.

The electronic anti-Stokes Raman scattering of the nantenna is enhanced by the junction plasmon. The signal strength decays when the junction fuses. An example of what appears as a catastrophic decay of the $t = 0$ signal is shown in Figure 6 (gray trace). The junction collapses after an induction period of ~15 s, which underscores that peak intensity arguments alone do not explain the damage. Evidently, irradiation-induced slow evolution of the junction, e.g., through thermal and electromigration induced mobility of surface atoms, precedes the catastrophic decay.

Mechanisms of Signal Degradation. We interrogate the integrity of the nantenna through the anti-Stokes ERS and that of its molecular load through SERS recorded during femtosecond laser irradiation. Large variations in behavior are observed on different structures under similar excitation conditions. Examples that illustrate prototypical mechanisms of signal decay are presented in Figure 7A–D. The variation in the rate of decay of the molecular SERS is illustrated in Figure 7A by the intensity of the 1640 cm^{-1} line. With time resolution limited by the SERS acquisition time to 1 s, the observed decay profiles range from sudden to gradual, from seconds to many minutes. The latter represent the survivors that live long enough to be measured. We also show before and after SERS spectra in Figure 7B, to highlight that in addition to decay of the parent spectrum, we see instances of plasmon-driven chemistry by the appearance of an unfamiliar new molecular spectrum (Figure 7B, top panel). In the SERS trajectory of Figure 7C, within one frame at $t = 0$, we see the disappearance of the BPE spectrum and appearance of the CN dissociation product, in what appears to be plasmon-driven rupture of the parent pyridine rings. The excitation is at 800 nm, at a local intensity nearing $I_{L,max} \sim 10^{13}$ W/cm^2, in the strong field limit of 8 V/nm. In the SERS trajectory of Figure 7D, recorded under similar conditions, arcing across the junction by the charge-transfer plasmon can be identified by the jumps in the ERS continuum. Such arcing events are also seen under cw excitation, at local fields of ~0.1 V/nm.[40] Arcing is typically followed by fluctuations in the molecular SERS spectra, as is evident in the trajectory at $t = 80$–100 s (Figure 7D). Among the variety of processes that occur in the strong field limit, we can identify internal field emission (arcing), plasmon-driven ionization, photodissociation, and separation of the molecule(s) from the hot spot while maintaining its identity.

Local Intensity Limit. The extensive exploration of intensities at which the signal decays is summarized in Figure 8, as a function of the fill factor. Within the order of magnitude uncertainty associated with defining damage thresholds, we see a well-defined limit in incident field intensities of 10^8 W/cm^2. Under the assumption of a common field enhancement factor $\beta = 100$, tolerable local fields of 10^{12}–10^{13} W/cm^2 is established. In effect, detectability in time-resolved measurements, as given in eq 4, is subject to the fundamental strong field limit:[41]

$$I_{L,max}^{peak} < 10^{12}\text{–}10^{13}\ \text{W/cm}^2 \quad (8)$$

DOI: 10.1021/acs.jpcc.6b02760
J. Phys. Chem. C 2016, 120, 20943–20953

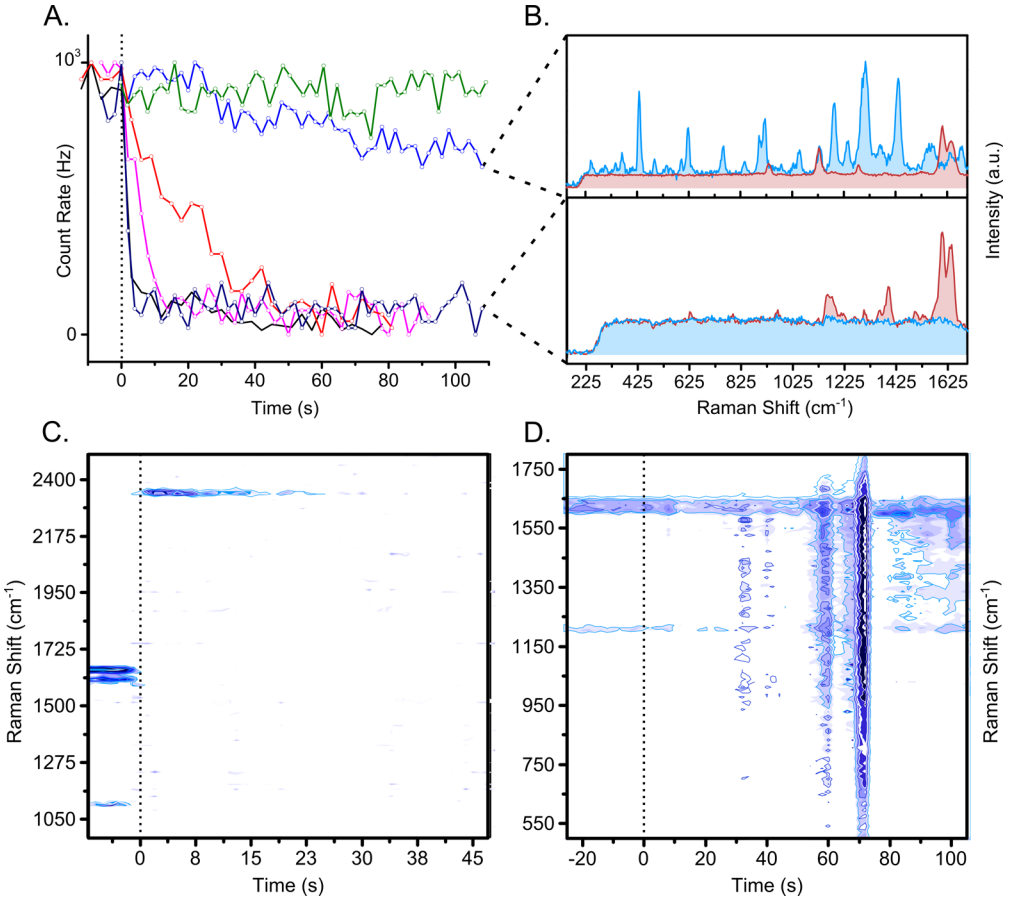

Figure 7. (A) Set of decay profiles taken on different nantennas depicting the evolution of the 1640 cm^{-1} line, during femtosecond irradiation: 610 nm, 100 fs pulses, 1−5 $\mu W/\mu m^2$ at 79 MHz (purple, black, and blue traces); and 50−100 $nW/\mu m^2$ at 250 kHz (red, olive, and cyan traces). (B) Pre- and post- femtosecond irradiation SERS spectra shown in red and blue, respectively. Top plot in panel B illustrates the generation of an unfamiliar spectrum; bottom plot in panelB illustrates loss of the molecular signal and preservation of the ERS background. (C, D) SERS trajectories, consisting of sequentially recorded spectra at a rate of 1 frame/s, acquired during femtosecond laser irradiation, highlighting distinctive behaviors: (C) the disappearance of the molecular signature concomitant with the appearance of a new line assigned to CN and (D) arcing through a junction as discerned by jumps in the ERS continuum.

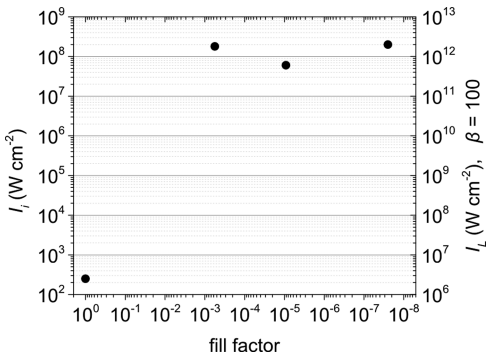

Figure 8. Measured tolerable incident and local intensity versus fill factor for an assumed value of $\beta = 100$.

Field enhancement reduces the demand on the incident intensity. Because stimulated steps are easily saturated (eq 7), rather than the β^8 enhancement suggested by eq 6, detectability in time-resolved SECARS reduces to the consideration of eq 5; namely, the quadratic enhancement of the spontaneous cross section and maximizing the fill factor. The latter is subject to yet another limitation, namely, heating and melting of the nantenna, which is the origin of the dramatic contrast between cw (ff = 1) and pulsed excitation intensity limits seen in Figure 8. Independence of the damage threshold on ff implies that the system cools between pulses.

Heating in Pulsed and Continuous Wave Irradiation. Heating of the nantenna can be conveniently monitored through the anti-Stokes ERS (Figure 2). The fit of the anti-Stokes spectrum to the Fermi−Dirac distribution yields the steady-state temperature of the nantenna. The cooling rate, dQ/dt, is then obtained from the measured steady-state temperature and the calculated absorption cross section (σ_a):

$$\frac{mC_p\Delta T}{\tau} = I_{0,cw}\sigma_a \tag{9}$$

From the slope of the experimental ΔT vs I plot,[42] we extract $\tau\sigma_a/mC_p = 10^6$ K μm^2/W, which yields a cooling time constant of $\tau = 25$ ns ($m = 2 \times 10^{-14}$ g, $\sigma = 10^{-9}$ $cm^2 = 0.1$ μm^2, $C_p = 0.129$ $J\,g^{-1}\,K^{-1}$). The long cooling time reflects the poor thermal conductivity of the silica shell. This can be recognized by estimating the rates of heat transfer from gold to silica and heat transport within the shell. Assuming contact between the metal and its surrounding shell, the heat exchange time, τ_{xc}, may be obtained by setting $VC_p = AlC_s$, where A is the surface area and $l = (D\tau)^{1/2}$ is the thermal diffusion length. For a nanosphere, this leads to

DOI: 10.1021/acs.jpcc.6b02760
J. Phys. Chem. C 2016, 120, 20943−20953

$$\tau_{xc} = \left(\frac{1}{D_s}\right)\left(\frac{r}{3}\frac{\rho_{Au}C_{Au}}{\rho_s C_s}\right)^2 \quad (10)$$

τ_{xc} = 0.3 ns for a shell consisting of crystalline quartz, τ_{xc} = 1.2 ns for glass, and longer for porous silica. Using conductivity of glass,[29] the time for heat to diffuse across the L = 70 nm shell is $\tau = L^2/D$ = 14 ns ($D = 3.4 \times 10^{-7}$ m^2/s), in agreement with the measured cooling time of 25 ns. Heat diffusion through the shell limits the rate of cooling in these dry-mounted, encapsulated nanostructures.

The heat load under cw irradiation, given by eq 9, is modified in pulsed excitation to

$$\Delta T(t) = \frac{I_{0,cw}\sigma_a}{mC_p}\frac{1}{f}\sum_n \Theta(t - n/f)\exp\left[-\frac{t - n/f}{\tau}\right] \quad (11)$$

in which Θ is the Heaviside function and τ is the cooling time constant. The steady-state temperature can be obtained as

$$\langle \Delta T\rangle = \frac{1}{t'}\int_{t_i}^{t_i+t'} \Delta T(t)\,dt \sim \frac{I_{0,cw}\sigma_a}{mC_p}\frac{1}{f}\mathrm{ff} = \frac{I_{0,cw}\sigma_a \delta t}{mC_p} \quad (12)$$

to recognize that the temperature is dictated by the pulse duration δt in this limit.

We should note that despite the large temperature rise, the gross shape of the nantenna is verifiably preserved by the silica shell until reaching average intensities of 1 mW/μm^2, where phase explosion is observed.[25] Spectral instabilities set in earlier (at 100 μW/μm^2 at 532 nm). As a general principle, the onset of bulk diffusion (of vacancies) in atomic solids can be taken as $T_{MP}/3$ = 450 K for gold and significantly lower for surface diffusion. Note that a single gold atom injected in a 1 nm junction gap constitutes a tunneling bridge that may shunt the displacement current. This would explain the observed arcing and catastrophic collapse of the junction after a period of irradiation (Figure 6). Also, large variations in β occur at junction gaps that range between 1 and 0.5 nm, which explain large fluctuations in signal that arise during fusion of the gap. Under ambient conditions, given the bulk diffusion rate, the requirement of ΔT_{max}= 150 K may be used to define the tolerable average power of irradiation:

$$I_0 = I_0\mathrm{ff} < mC_p\Delta T_{max}/\sigma_a(\omega)\delta t \quad (13)$$

This translates to 100 μW/μm^2 at 532 nm (ff = 1), and knowledge of the wavelength-dependent absorption cross section (Figure 1) allows generalization of eq 13 to different excitation colors.

CONCLUSIONS

The ν-domain ps-SECARS measurements carried out on single plasmonic nanonatennas illustrate coherent Raman spectroscopy in the few-molecule limit. The recorded spectra are undersampled copies of the cw-SERS spectra. This is in contrast with the fs-SRS measurements on the same system, which show dispersive lines.[22] The contrast is remarkable because it does not follow expectations based on ensemble measurements. Beside the distinction that the CARS signal cannot interfere with the incident fields, due to its color and scattering geometry, an important distinction is the time ordering of interactions. In SRS, the incident field drives the nantenna, which in turn excites the molecule, and the reradiation of the molecule is amplified by the nantenna. We have shown that ultrafast SECARS on single scattering centers can be understood as a saturated SRS step, followed by surface-enhanced, spontaneous anti-Stokes Raman scattering. Because the final step in which the signal is formed is the same as in SERS, it is perhaps not surprising that the observed line profiles are the same. However, in both SERS and SECARS there is an interplay between the molecular response, ERS of the nantenna, and coupled molecule−metal scattering, which depends strongly on the selected excitation resonances.

The contrast between the line profiles observed in the present ν-domain ps-SECARS measurements and those implied by the prior t-domain fs-SECARS measurements underscores that in the few-molecule limit, the two measurements are not Fourier-related. The t-domain CARS yields the cross-correlation among the members of the prepared vibrational superposition, while the ν-domain measurements yield the autocorrelation of individual vibrational lines. Hence, in the few-molecule limit, the t-domain measurement reveals cross-correlation information that cannot be directly extracted from ν-domain measurements, allowing a more in-depth interrogation of molecular dynamics. The two are identical in the limit of large ensembles, where the tr-CARS signal can be retrieved through a Fourier transform of the Raman spectrum.[35]

More generally, we explore the parameter space for designing tr-SE-NLO. We show that stimulated steps are easily saturated; as such, tr-SECARS and tr-SERS scattering rates are determined by the final spontaneous radiation cross section, which in turn is quadratically enhanced: $\sigma_s^* = \beta_s^2\sigma_s$. This is to be contrasted with the effective quartic, β^4, enhancement in cw SERS and the naïve extrapolation that in the four-photon CARS process one may expect β^8 enhancement. The quadratic enhancement of incident fields $I_L = \beta_i^2 I_i$ has the primary advantage of lowering the demand on incident intensity. The combination of field enhancement and tight focusing requirements to isolate single scattering centers leads to limiting strong local fields 10^{12}−10^{13} W/cm^2 with what may be regarded as weak laser source: 100 fJ per 100 fs pulse (100 μW at 10^8 Hz). For typical nonresonant molecular scatterers, due to the reduced duty cycle of pulsed lasers, the dynamic range between observation and damage threshold is rather limited. In effect, enhancement factors that dictate the sensitivity of SERS can be detrimental in ultrafast measurements. The variety of chemical and physical processes that compete at these high field intensities were illustrated through examples. In this regard, the encapsulated nanosphere dimer is well suited to interrogate plasmonic chemistry in isolation. Beside the fundamental limits in both peak and average intensities that we extract from a large number of measurements on single nantennas, we point out that an effective mode-matching criterion exists in multicolor experiments. The latter consideration, namely, the role of the spatial and temporal coherence of plasmons in coherent Raman scattering, deserves further exploration.

AUTHOR INFORMATION

Corresponding Authors

*E-mail: epotma@uci.edu. Tel.: 949-824-9942.
*E-mail: aapkaria@uci.edu. Tel.: 949-824-6851.

Present Address

‖A.Z.: Technology and Applications Center, Newport Corporation, Irvine, CA 92606.

DOI: 10.1021/acs.jpcc.6b02760
J. Phys. Chem. C 2016, 120, 20943−20953

Notes

The authors declare no competing financial interest.

■ ACKNOWLEDGMENTS

This research was made possible through the NSF Center for Chemistry at the Space-Time Limit (CaSTL), through Grant CHE-1414466. We thank G. C. Schatz and R. P. Van Duyne for sharing their analysis of fs-SRS results on the same system prior to publication.

■ REFERENCES

(1) Novotny, L.; van Hulst, N. Antennas for Light. *Nat. Photonics* **2011**, *5*, 83−90.
(2) Hua, X.; Voronine, D. V.; Ballmann, C. W.; Sinyukov, A. M.; Sokolov, A. V.; Scully, M. O. Nature of Surface-Enhanced Coherent Raman Scattering. *Phys. Rev. A: At., Mol., Opt. Phys.* **2014**, *89*, 043841.
(3) Nie, S.; Emory, S. R. Probing Single Molecules and Single Nanoparticles by Surface-Enhanced Raman Scattering. *Science* **1997**, *275*, 1102−1106.
(4) Kneipp, K.; Moskovits, M.; Kneipp, H. *Surface Enhanced Raman Scattering, Physics and Applications*; Springer: Berlin, 2006; Vol. *103*.
(5) Dieringer, J. A.; Lettan, R. B., II; Scheidt, K. A.; Van Duyne, R. P. A Frequency Domain Existence Proof of Single-Molecule Surface-Enhanced Raman Spectroscopy. *J. Am. Chem. Soc.* **2007**, *129*, 16249−56.
(6) Arroyo, J. O.; Kukura, P. Non-Fluorescent Schemes for Single-Molecule Detection, Imaging and Spectroscopy. *Nat. Photonics* **2016**, *10*, 11−17.
(7) Frontiera, R. R.; Gruenke, N. L.; Van Duyne, R. P. Fano-Like Resonances Arising from Long-Lived Molecule-Plasmon Interactions in Colloidal Nanoantennas. *Nano Lett.* **2012**, *12*, 5989−5994.
(8) Klingsporn, J. M.; Sonntag, M. D.; Seideman, T.; Van Duyne, R. P. Tip-Enhanced Raman Spectroscopy with Picosecond Pulses. *J. Phys. Chem. Lett.* **2014**, *5*, 106−10.
(9) Chen, C. K.; Heinz, T. F.; Ricard, D.; Shen, Y. R. Surface-Enhanced Second-Harmonic Generation and Raman Scattering. *Phys. Rev. B: Condens. Matter Mater. Phys.* **1983**, *27*, 1965−1979.
(10) Danckwerts, M.; Novotny, L. Optical Frequency Mixing at Coupled Gold Nanoparticles. *Phys. Rev. Lett.* **2007**, *98*, 026104.
(11) Renger, J.; Quidant, R.; van Hulst, N.; Novotny, L. Surface-Enhanced Nonlinear Four-Wave Mixing. *Phys. Rev. Lett.* **2010**, *104*, 046803.
(12) Wang, Y.; Lin, C.-Y.; Nikolaenko, A.; Raghunathan, V.; Potma, E. O. Four-Wave Mixing Microscopy of Nanostructures. *Adv. Opt. Photonics* **2011**, *3*, 1−52.
(13) Zhang, Y.; Wen, F.; Zhen, Y. R.; Nordlander, P.; Halas, N. J. Coherent Fano Resonances in a Plasmonic Nanocluster Enhance Optical Four-Wave Mixing. *Proc. Natl. Acad. Sci. U. S. A.* **2013**, *110*, 9215−9.
(14) Gruenke, N. L.; Cardinal, M. F.; McAnally, M. O.; Frontiera, R. R.; Schatz, G. C.; Van Duyne, R. P. Ultrafast and Nonlinear Surface-Enhanced Raman Spectroscopy. *Chem. Soc. Rev.* **2016**, *45*, 2263−2290.
(15) Koo, T.-W.; Chan, S.; Berlin, A. A. Single-Molecule Detection of Biomolecules by Surface-Enhanced Coherent Anti-Stokes Raman Scattering. *Opt. Lett.* **2005**, *30*, 1024−1026.
(16) Liang, E. J.; Weippert, A.; Funk, J. M.; Materny, A.; Kiefer, W. Experimental Observation of Surface-Enhanced Coherent Anti-Stokes Raman Scattering. *Chem. Phys. Lett.* **1994**, *227*, 115−120.
(17) Ichimura, T.; Hayazawa, N.; Hashimoto, M.; Inouye, Y.; Kawata, S. Tip-Enhanced Coherent Anti-Stokes Raman Scattering for Vibrational Nanoimaging. *Phys. Rev. Lett.* **2004**, *92*, 220801.
(18) Namboodiri, V.; Namboodiri, M.; Diaz, G. I. C.; Oppermann, M.; Flachenecker, G.; Materny, A. Surface-Enhanced Femtosecond Cars Spectroscopy (Se-Cars) on Pyridine. *Vib. Spectrosc.* **2011**, *56*, 9−12.
(19) Steuwe, C.; Kaminski, C. F.; Baumberg, J. J.; Mahajan, S. Surface Enhanced Coherent Anti-Stokes Raman Scattering on Nanostructured Gold Surfaces. *Nano Lett.* **2011**, *11*, 5339−5343.
(20) Zhang, Y.; Zhen, Y. R.; Neumann, O.; Day, J. K.; Nordlander, P.; Halas, N. J. Coherent Anti-Stokes Raman Scattering with Single-Molecule Sensitivity Using a Plasmonic Fano Resonance. *Nat. Commun.* **2014**, *5*, 4424.
(21) Voronine, D. V.; Sinyukov, A. M.; Hua, X.; Wang, K.; Jha, P. K.; Munusamy, E.; Wheeler, S. E.; Welch, G.; Sokolov, A. V.; Scully, M. O. Time-Resolved Surface-Enhanced Coherent Sensing of Nanoscale Molecular Complexes. *Sci. Rep.* **2012**, *2*, 891.
(22) Frontiera, R. R.; Henry, A.-I.; Gruenke, N. L.; Van Duyne, R. P. Surface-Enhanced Femtosecond Stimulated Raman Spectroscopy. *J. Phys. Chem. Lett.* **2011**, *2*, 1199−1203.
(23) Voronine, D. V.; Sinyukov, A. M.; Hua, X.; Munusamy, E.; Ariunbold, G.; Sokolov, A. V.; Scully, M. O. Complex Line Shapes in Surface-Enhanced Coherent Raman Spectroscopy. *J. Mod. Opt.* **2015**, *62*, 90−96.
(24) Eesley, G. L. *Coherent Raman Spectroscopy*; Pergamon Press: Oxford, NY, 1981.
(25) Yampolsky, S.; Fishman, D. A.; Dey, S.; Hulkko, E.; Banik, M.; Potma, E. O.; Apkarian, V. A. Seeing a Single Molecule Vibrate Through Time-Resolved Coherent Anti-Stokes Raman Scattering. *Nat. Photonics* **2014**, *8*, 650−656.
(26) Marhaba, S.; Bachelier, G.; Bonnet, C.; Broyer, M.; Cottancin, E.; Grillet, N.; Lermé, J.; Vialle, J.-L.; Pellarin, M. Surface Plasmon Resonance of Single Gold Nanodimers Near the Conductive Contact Limit. *J. Phys. Chem. C* **2009**, *113*, 4349−4356.
(27) Nordlander, P.; Oubre, C.; Prodan, E.; Li, K.; Stockman, M. I. Plasmon Hybridization in Nanoparticle Dimers. *Nano Lett.* **2004**, *4*, 899−903.
(28) Olmon, R. L.; Slovick, B.; Johnson, T. W.; Shelton, D.; Oh, S.-H.; Boreman, G. D.; Raschke, M. B. Optical Dielectric Function of Gold. *Phys. Rev. B: Condens. Matter Mater. Phys.* **2012**, *86*, 235147.
(29) Malitson, I. H. Interspecimen Comparison of the Refractive Index of Fused Silica. *J. Opt. Soc. Am.* **1965**, *55*, 1205.
(30) Yang, W. H.; Hulteen, J.; Schatz, G. C.; Van Duyne, R. P. A Surface-Enhanced Hyper-Raman and Surface-Enhanced Raman Scattering Study of Trans-1,2-Bis(4-Pyridyl)Ethylene Adsorbed Onto Silver Film Over Nanosphere Electrodes. Vibrational Assignments: Experiment and Theory. *J. Chem. Phys.* **1996**, *104*, 4313−4323.
(31) Dey, S.; Banik, M.; Hulkko, E.; Rodriguez, K.; Apkarian, V. A.; Galperin, M.; Nitzan, A. Observation and Analysis of Fano-Like Lineshapes in the Raman Spectra of Molecules Adsorbed at Metal Interfaces. *Phys. Rev. B: Condens. Matter Mater. Phys.* **2016**, *93*, 035411.
(32) Hugall, J. T.; Baumberg, J. J. Demonstrating Photoluminescence from Au Is Electronic Inelastic Light Scattering of a Plasmonic Metal: The Origin of Sers Backgrounds. *Nano Lett.* **2015**, *15*, 2600−2604.
(33) Banik, M. *SERS from the Point of View of the Molecule & the Antenna*. Ph.D. Disseration, University of California, Irvine, CA, 2014.
(34) Blackie, E. J.; Ru, E. C. L.; Etchegoin, P. G. Single-Molecule Surface-Enhanced Raman Spectroscopy of Nonresonant Molecules. *J. Am. Chem. Soc.* **2009**, *131*, 14466−1472.
(35) Zeytunyan, A.; Crampton, K. T.; Zadoyan, R.; Apkarian, V. A. Supercontinuum-Based Three-Color Three-Pulse Time-Resolved Coherent Anti-Stokes Raman Scattering. *Opt. Express* **2015**, *23*, 24019.
(36) Mukamel, S. *Principles of Nonlinear Optical Spectroscopy*; Oxford University Press: New York, 1995.
(37) Zadoyan, R.; Apkarian, V. A. Imaging the Molecular Rovibrational Coherence Through Time-Gated, Frequency-Resolved Coherent Anti-Stokes Raman Scattering. *Chem. Phys. Lett.* **2000**, *326*, 1−10.
(38) Schatz, G. C.; Ratner, M. A. *Quantum Mechanics in Chemistry*; Dover Publications: Mineola, NY, 1993.
(39) Silva, W. R.; Graefe, C. T.; Frontiera, R. R. Toward Label-Free Super-Resolution Microscopy. *ACS Photonics* **2016**, *3*, 79−86.
(40) El-Khoury, P. Z.; Hu, D.; Apkarian, V. A.; Hess, W. P. Raman Scattering at Plasmonic Junctions Shorted by Conductive Molecular Bridges. *Nano Lett.* **2013**, *13*, 1858−1861.
(41) Keldysh, L. V. Ionization in the Field of a Strong Electromagnetic Wave. *Sov. Phys. JETP* **1965**, *5*, 1307−1314.

DOI: 10.1021/acs.jpcc.6b02760
J. Phys. Chem. C 2016, 120, 20943−20953

(42) Banik, M.; Apkarian, V. A.; Park, T. H.; Galperin, M. Raman Staircase in Charge Transfer Sers at the Junction of Fusing Nanospheres. *J. Phys. Chem. Lett.* **2013**, *4*, 88−92.

DOI: 10.1021/acs.jpcc.6b02760
J. Phys. Chem. C 2016, 120, 20943−20953